Sensors and Materials, Vol. 36, No. 6 (2024) 2351–2370
MYU Tokyo

S & M 3673

A Novel Design of a Small Adaptive Bionic Obstacle-crossing Vehicle

Gang Chen,[1] Kun-Chieh Wang,[1*] Lei Wu,[1] and Shi-Yun Zhan[2]

[1]School of Mechanical and Electric Engineering, Sanming University, Sanming, Fujian Province 365004, China
[2]Sinotruk Fujian Haixi Automobile Co., Ltd., Yongan, Fujian Yong'an City Po Ling 99, Fujian Province, China

(Received January 3, 2024; accepted May 27, 2024)

Keywords: disaster rescue, obstacle-crossing rover, adaptive control, bionic vehicle design

To improve the efficiency of postdisaster victim detection and rescue, especially in narrow spaces and dangerous areas difficult for rescue personnel to reach, a small obstacle-crossing vehicle (OCV) with high-precision sensing ability and terrain motion adaptability is needed. To this end, we designed a novel adaptive OCV based on bionics for postdisaster detection and rescue work. The major work we have performed in this study includes the planning of bionic gaits, the motion analysis of the vehicle mechanism, the application of high-precision sensors in vehicles, the development of an adaptive compound control method, and the structural finite element simulation. Finally, the designed bionic OCV walking verification tests were carried out on seven different obstacle roadways, and satisfactory results were obtained. The feature of this study is a bionic OCV compound obstacle control method and strategy with high adaptability. The novelty of this study is that our proposed OCV bionic gait planning includes strategies to cope with the complex and changeable road terrain environment, and the proposed compound obstacle control method has the characteristics of high accuracy and strong adaptability in controlling OCV obstacle movement.

1. Introduction

Natural and manmade disasters frequently threaten the safety of human life and property. In some sudden disasters, for example, fire may cause explosion at any time, buildings will collapse after an earthquake, and toxic substances will spread and leak everywhere, which prevents relief workers from entering the scene of the disaster. However, the small obstacle-crossing vehicle (OCV) can replace rescue workers in carrying out search and rescue tasks, reducing the casualties amoung the rescue workers.[1–4] Road conditions have a considerable effect on the driving stability of OCVs. Owing to complicated road conditions, the obstacle-crossing ability is the key issue focused on by rover researchers.[5,6] How to restrain interference and maintain the stability of the vehicle body significantly determine the obstacle-crossing ability of a rover.[7–9]

In the last decade, the unmanned ground vehicle (UGV) has been widely used in military, industry, and other special fields because of its high automatic control and adaptive and maneuvering abilities. Since UGV usually performs tasks in various terrain environments, all-

*Corresponding author: e-mail: m18316252102@126.com
https://doi.org/10.18494/SAM4879

ISSN 0914-4935

terrain motion adaptability has become an indicator of a UGV's efficiency and reliability. For example, He *et al.*[10] investigated the related dynamic characteristics of an obstacle-crossing UGV. Zhang *et al.*[11] designed a bidirectional six-wheel planetary rover for road conditions on rugged planetary surfaces. Because of the coordinated movement of specially designed brake structures and electric push levers, this rover has a dual-drive obstacle-crossing ability. Wang *et al.*[12] designed a road-crossing vehicle with variable configuration, and analyzed the effects of wheel weight and suspension stiffness on its road-crossing ability using statistical methods. They experimentally verified that the designed vehicle was able to cross a 1-m-high step obstacle. Wang *et al.*[13] proposed the obstacle-crossing performance index of a mobile robot considering difficult road conditions, such as roads with deep trenches, steep slope topography, and stepped landform. Meanwhile, they carried out a simulation study on the obstacle-crossing ability of the mobile robot using Automatic Dynamic Analysis of Mechanical System (ADAMS) software. Xu *et al.*[14] proposed a new stability control method of the chassis of a wheeled vehicle traveling on rough terrain to improve its attitude tracking performance. In addition, they verified the effectiveness and robustness of the proposed control method through a series of numerical tests, and found that the stability of the robot in motion is satisfactory. Chen and Yu[15] developed a new eight-wheel-drive OCV using the variable structure design method with the scheme of a variable center of gravity. They studied the motion principle of climbing vertical steps for an OCV using the D'Alembert method, adopted a new active-adjusting control strategy for crossing obstacles, and established a motion model via simulations using ADAMS software. Leng *et al.*[16] developed an electric mining vehicle (EMV) adapted to the complex seabed terrain environment, analyzed the obstacle crossing process and the variation rule of the output torque of the EMV, and performed force analysis via Swanson Analysis Systems, Inc. (ANSY) simulations. Hao *et al.*[17] proposed a six-wheel vehicle chassis with a variable wheelbase. Through mechanical analyses, they studied the effect of the wheelbase on the maximum height of an obstacle that the vehicle can cross and obtained the numerical relationship between the wheelbase and the obstacle height via numerical calculations.

From the above literature survey, it is certain that all aspects of OCVs still need to be improved, including miniaturizing its body, improving its sensing accuracy for various road conditions, increasing its obstacle-crossing ability for various rough terrains, and developing new adaptive control methods. Therefore, we designed a novel OCV on the basis of bionic motion principles. We analyzed its movement through experimental verification to address the aforementioned issue. The main tasks include designing bionic gaits, analyzing the motion of the OCV mechanism, integrating high-precision sensors into the vehicle, developing an adaptive compound control method, and conducting structural finite element analysis (FEA). Finally, we verified the obstacle-crossing performance of the proposed bionic OCV on seven different complex terrain roads.

2. Design and Working Principle of Bionic OCV

2.1 Mechanical design

Wheeled OCVs have the characteristics of simple structure, fast running, good obstacle-crossing ability, and simple control but poor stability.[18] To solve this instability problem, we developed a novel adaptive bionic OCV on the basis of the hybrid concept of a basic wheeled-type rover structure and a biomimetic mechanism that can simulate the climbing motion of an animal. Since different OCVs have different mechanism features, we now discuss how to design the optimal mechanism of an OCV on the basis of five performance aspects—structural complexity, running speed, stability, obstacle-crossing ability, and degree of difficulty of control—as discussed below.[19]

(1) The structural complexity of the OCV decreases as the number of parts used to complete the same task with the same motion performance decreases.
(2) Running speed means that under the same task conditions, the shorter the completion time, the higher the completion efficiency, and the faster the running speed of the OCV.
(3) A stable OCV means that during the process of crossing the obstacle, the swing amplitude of the entire OCV body cannot be too large, and problems such as tilt and rollover will not easily occur.
(4) Obstacle-crossing ability refers to the ability of the OCV to climb over obstacles, and it is impermissible to stop, stall, or get stuck during climbing.
(5) The degree of difficulty of control refers to the extent of how easily an OCV can perform the specified action with the designed controller.

Table 1 lists the performance comparisons of the four commonly used OCVs. It is found that the wheeled-type obstacle-crossing rover has simple structures, fast running speed, and good obstacle-crossing ability, and is much easier to control, but has poor stability. In contrast, the hybrid-type obstacle-crossing rover has better stability and retains most of its advantages. Therefore, we chose the structure of a wheeled-type OCV as the design base and combined it with an animal-mimicking climbing mechanism to form a novel bionic OCV.

The motion mechanisms of our designed bionic OCV are divided into three major parts. The front and rear parts are used for climbing motion, and the middle part is used for walking and driving motions. Each wheel is driven by a deceleration motor, and the auxiliary arm is powered by a remote control (RC) motor to perform the up and down swinging action. The structure of the designed bionic OCV is schematically shown in Fig. 1.

Table 1
Different types of OCV.

Function	Car type			
	Wheeled	Tracked	Leg	Mixed
Complexity	Low	Middle	Middle	High
Speed	High	Middle	Low	High
Stability	Bad	Good	Bad	Middle
Obstacle climbing	Good	Bad	Good	Good
Easy control	Good	Good	Bad	Bad

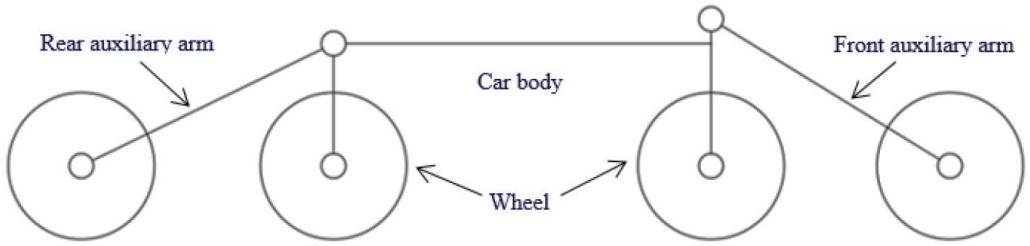

Fig. 1. Schematic diagram of the designed bionic OCV.

When the front side of the designed bionic OCV encounters an obstacle, the two front wheels are raised by the front RC motor and the two rear wheels are lowered by the rear RC motor. With the continuous movement of the OCV, when its two front wheels reach the top of the obstacle, the front RC motor begins to turn downward and the front auxiliary arm is pressed down; meanwhile, the rear RC motor is turned upward and the rear auxiliary arm is lifted up; finally the OCV crosses the obstacle. The structure of the front auxiliary arm is shown in Fig. 2(a). To increase the ground clearance and improve the obstacle-crossing ability, the driving motor of the front wheel is installed vertically, as shown in Fig. 2(b).

To firmly attach all parts of the bionic OCV to its main body, we used hexagonal screws to fix the front and rear auxiliary arms to the front and rear ends, respectively, of the vehicle body, and a rudder is connected between the RC motor and the vehicle body. With this rudder, we can not only achieve the fixation of the parts, but also perform the up and down swinging motion of the front and rear auxiliary arms. We adopted six prismatic columns as the supporting structure between the car body and the wheel legs in which they not only improved the height of the whole car body, but also ensured good road passability. The overall assembly of our designed bionic OCV is shown in Fig. 3.

2.2 Key component designs

We now discuss the design of three key components in the proposed OCV: motor, sensor, and controller.

2.2.1. Driving motor

Our designed OCV has a body mass (M_1) of 1.5 ± 0.5 kg, and each wheel has the mass (m) of 0.035 kg and the diameter (d) of 62 mm. It is assumed that the friction coefficient (φ) between the car wheel and the ground is 0.71, the acceleration of gravity (g) is 9.8 m/s^2, and the motor power loss is neglected.

2.2.1.1 Power required in plane motion

When moving on the flat ground, there are six wheels touching the ground at the same time. We assume that the driving force of the motor can be evenly distributed to the six wheels. The normal force acting on each wheel can be calculated as

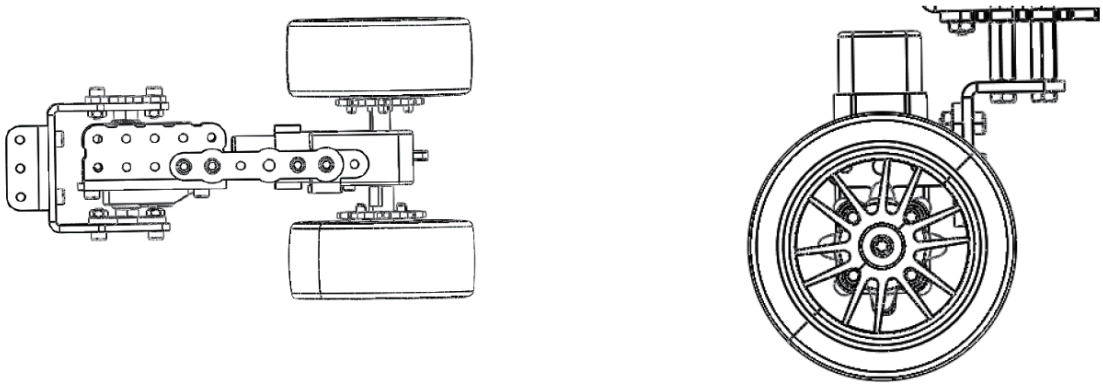

(a) (b)

Fig. 2. Main components of bionic OCV: (a) structure of front auxiliary arm; (b) structure of front wheel leg with driving motor.

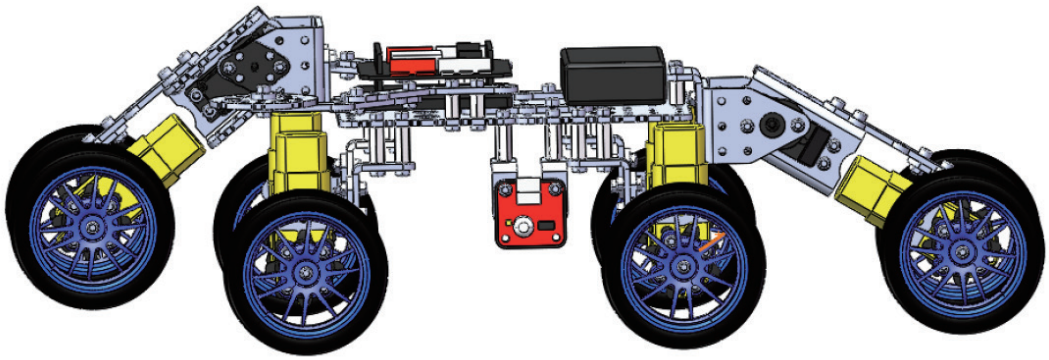

Fig. 3. (Color online) Overall assembly of designed bionic OCV.

$$N = \frac{1}{6}(M + 6m) \cdot g. \tag{1}$$

The friction force of each wheel is expressed as

$$F_{\varphi} = N \cdot \varphi. \tag{2}$$

The maximum rotational speed of each wheel is calculated as

$$n_1 = \frac{60 v_1}{\pi d}. \tag{3}$$

From the above data and Eq. (3), we obtain the maximum speed of the wheel as v_1 = 0.5 m/s. The torque received by the wheel can be calculated from

$$T_1 = F_\varphi \cdot \frac{d}{2}. \tag{4}$$

The power required by the driving motor is calculated as

$$P_1 = \frac{T_1 \cdot n_1}{9550}. \tag{5}$$

Eventually, we obtain the power required for the designed bionic OCV moving on the flat ground as $P_1 = 0.992$ W.

2.2.1.2 Power required in stair-climbing motion

In the stair-climbing process, the designed bionic OCV must overcome the effect of gravity by doing work continuously; the required torque can be calculated as

$$T_2 = \frac{1}{6}(M + 6m)g \cdot L, \tag{6}$$

where L is the vertical distance between the wheel axis and the gravity lines. We assume that the maximum translation velocity of the OCV is $v_2 = 0.4$ m/s. The maximum rotational speed of the wheels can be calculated as

$$n_2 = \frac{60v_2}{\pi L}, \tag{7}$$

and the required driving power can be calculated as

$$P_2 = \frac{T_2 \cdot n_2}{9550}. \tag{8}$$

Thus, the obtained power is $P_2 = 2.235$ W.

It is seen that $P_2 > P_1$. For safety, the minimum required motor power can be chosen as $P = 3$ W. On the basis of the required power calculated above, we appropriately chose four single-axis and four dual-axis DC deceleration motors, as shown in Fig. 4. The four single-axis DC deceleration motors are used in the middle four wheels for translation driving, and the two dual-axis DC motors are used for the front and rear wheels for climb driving.

2.2.2 RC motor

In our design, the RC motor should be capable of providing enough torque to support the weight of the entire auxiliary arms, as well as freely rotating 360 degrees to drive the arm in

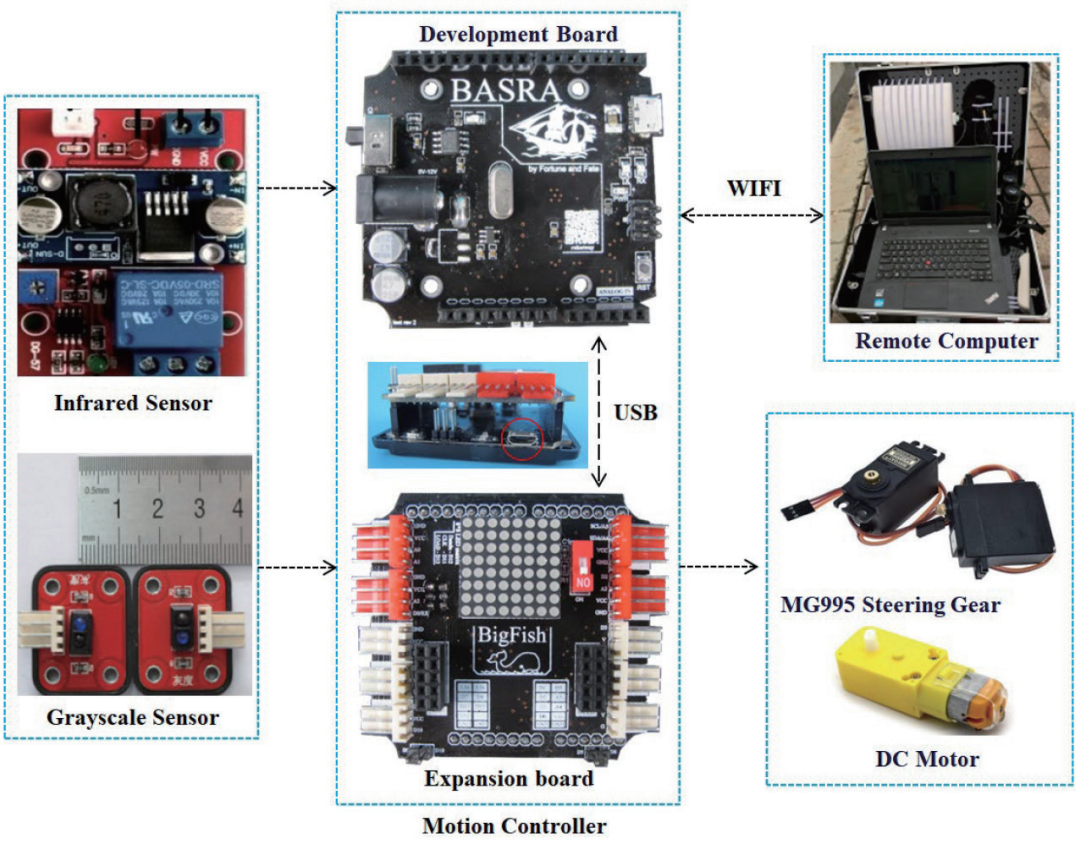

Fig. 4. (Color online) Arrangement of key components of bionic OCV.

swinging motions up and down. We now make a force analysis on the auxiliary arm system that mainly includes four parts: two wheels, two wheel driving motors, an arm body, and an RC motor. For the auxiliary arm system, the mass of a single wheel is $m_1 = 40$ g, the mass of a wheel driving motor is $m_2 = 50$ g, the overall length of the auxiliary arm system is $L = 115$ cm, the mass of the metal arm body is $m_3 = 200$ g, and the mass of the RC motor is $m_4 = 60$ g. From the viewpoint of force balance, we have

$$G = (2m_1 + m_2 + m_3 + m_4) \cdot g, \tag{9}$$

where G is the gravity force applied on the whole vehicle. The torque produced by the RC motor is calculated from

$$T = G \cdot L \tag{10}$$

and obtained as $M = 0.4395$ Nm. On the basis of safe running, we adopt the RC motor of Model MG995 with a maximum working torque of 2.0 Nm, as shown in Fig. 4.

2.2.3 Controller

We adopt two types of controller: Basra development board (BDP)[20] and Bigfish expansion board (BEB),[21] as shown in Fig. 4. The architecture of the BDP controller is an open-source-based Arduino system, which can detect the change of environment via various sensors such as grayscale sensors, infrared sensors, and ultrasonic sensors. The BDP controller has a core processor of ATmega328, a total of 14 digital input and output ports, and can be programmed using C language.

For BEB, there are four servo motor interfaces and six sensor interfaces located on its left and right sides, respectively, and two DC motor interfaces and a general extension interface located on its bottom. Moreover, the BEB is equipped with a driver chip of Model fan 8100mtc, which can drive two DC motors at the same time, and is also equipped with a USB driver chip and an automatic reset circuit, so that users can reset this board directly.

2.2.4 Sensor

We use two types of sensor in bionic OCV, an infrared sensor to detect obstacles on the road and a grayscale sensor to track vehicle trajectories, as shown in Fig. 4.

The adopted infrared sensor has a monitoring distance of 20 cm. We installed one infrared sensor on each side of the vehicle body. When the infrared emitted by the sensors detects an object, it will be received by the sensors after being reflected on the object, and the received signal will be transmitted to the controller, which will issue instructions to drive the vehicle to take corresponding actions.

On the other hand, the adopted grayscale sensor has an effective distance as large as 3 cm. To accurately detect the trajectory of the bionic OCV during movement, we used two grayscale sensors to identify the black line on the ground, with one installed on the left and the other installed on the right side of the vehicle body, so that the black lines can always be sandwiched between the two grayscale sensors. If the left grayscale sensor detects a black line, it means that the trajectory of the vehicle is offset to the right, away from the predetermined trajectory. At this moment, following the instructions sent by the controller, the vehicle will move to the left to correct its current trajectory. Similarly, if the right grayscale sensor detects a black line, the vehicle will be driven to the right for correction. Through this specific trajectory control with the aid of two grayscale sensors, the black line is always located between these two sensors, so that no deviation occurs while the vehicle is moving. Note that the distance between the grayscale sensor and the ground should be controlled within 1–3 cm to prevent it from being too far away to identify the black line.

2.3 Planning and analysis of OCV motion

2.3.1 Motion analysis

To reach the goal that the designed OCV can move quickly and steadily over obstacles, we simulated the climbing process of a four-limbed animal through the alternating up and down

swing of the front and rear auxiliary arms to cross the obstacle. Taking the case of the bionic OCV climbing a ladder as an example, we planned five-stage actions as described in the following and shown in Figs. 5(a)–5(f).

1st stage:

The front auxiliary arm of the bionic OCV begins to lift, and the lifting height exceeds the height of the first step, at which time the front wheels of the vehicle touch the first step, as shown in Figs. 5(a) and 5(b).

2nd stage:

The front auxiliary arm of the bionic OCV begins to press down, and the rear auxiliary arm begins to lift. At this time, the wheels of the front auxiliary arm come into contact with the upper part of the first step, the front wheels come into contact with the edge of the first step, the rear wheels are in a suspended state, and the wheels of the rear auxiliary arm come into contact with the ground. The whole body is in a balanced state under the support of the front and rear auxiliary arms, as shown in Figs. 5(c) and 5(d).

3rd stage:

The front auxiliary arm of the bionic OCV is in the state of downward pressure, and the rear auxiliary arm is subjected to an upward lift. At this time, the front wheels pass the first step and the rear wheels contact the ground, as shown in Fig. 5(d).

4th stage:

The front auxiliary arm of the bionic OCV is completely subjected to a downward pressure, and the rear auxiliary arm is subjected to a full upward lift. At this time, the wheels of the front

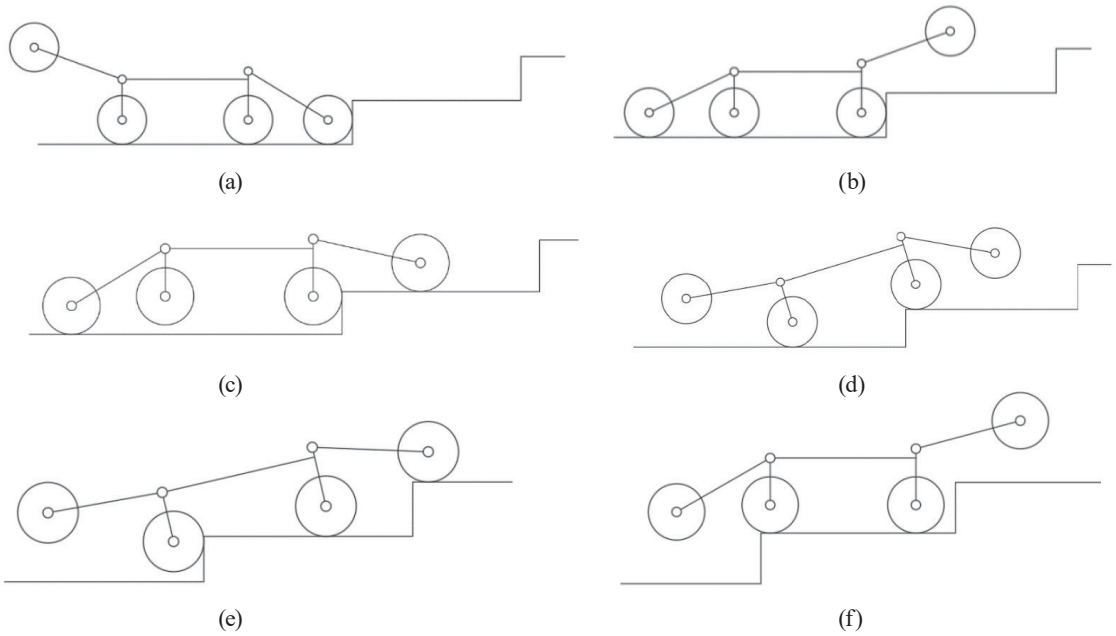

Fig. 5. Planning of climbing process of designed bionic OCV. (a) The front auxiliary arm wheels are in contact with the first step. (b) The front wheels are in contact with the first step. (c) The front auxiliary arm presses down and the rear auxiliary arm begins to lift. (d) The front and rear wheels touch the step and the ground, respectively, and the OCV moves forward. (e) The rear wheels touch the first step. (f) The bionic OCV completes the first-step climbing.

auxiliary arm come into contact with the second step, the front wheels come into contact with the upper part of the first step, and the wheels of the rear auxiliary arm come into contact with the edge of the first step, as shown in Fig. 5(e).

5th stage:

The bionic OCV has completely climbed the first step, at which time the front auxiliary arm begins to lift and the rear auxiliary arm begins to press down, as shown in Fig. 5(f). Thereafter, the bionic OCV continues to repeat the ladder climbing process and climb the next step.

2.3.2 Mechanical analysis

To fully understand the obstacle-crossing ability of our designed bionic OCV, the force analysis of OCV climbing the ladder is performed as below. The specific ladder we used has a width of 207 cm and a height of 54 cm. The force distributions of the proposed bionic OCV during the stair-climbing process are divided into three states, as described in the following and shown in Fig. 6.

State 1 [shown in Fig. 6(a)]:

The front auxiliary arm just starts to be pressed down, so that its wheels come into contact with the upper surface of the first step, and the rear auxiliary arm starts to be lifted.

(1) For the wheels of the rear auxiliary arm, the force balance equation in the *X* direction can be expressed as

$$F_{x1} - f_1 - F_{n1} \cdot \sin\alpha_1 = 0. \tag{11}$$

That in the *Y* direction can be expressed as

$$F_1 + F_{n1} \cdot \cos\alpha_1 - G_1 = 0, \tag{12}$$

where G_1 is the gravitational force of the rear wheels, F_1 is the ground-supporting force of the rear auxiliary arm, F_{x1} is the driving force of the wheels of the rear auxiliary arm, f_1 is the horizontal friction force between the rear wheels and the ground during movement, and F_{n1} is the upward force exerted by the RC motor with an angle of α_1 to the normal line through the wheel center.

(2) For the wheels of the front auxiliary arm, the force balance equation in the *X* direction can be expressed as

$$F_{x2} - f_2 - F_{n2} \cdot \sin\beta_1 = 0. \tag{13}$$

That in the *Y* direction can be expressed as

$$F_2 - F_{n2} \cdot \cos\beta_1 - G_2 = 0, \tag{14}$$

and

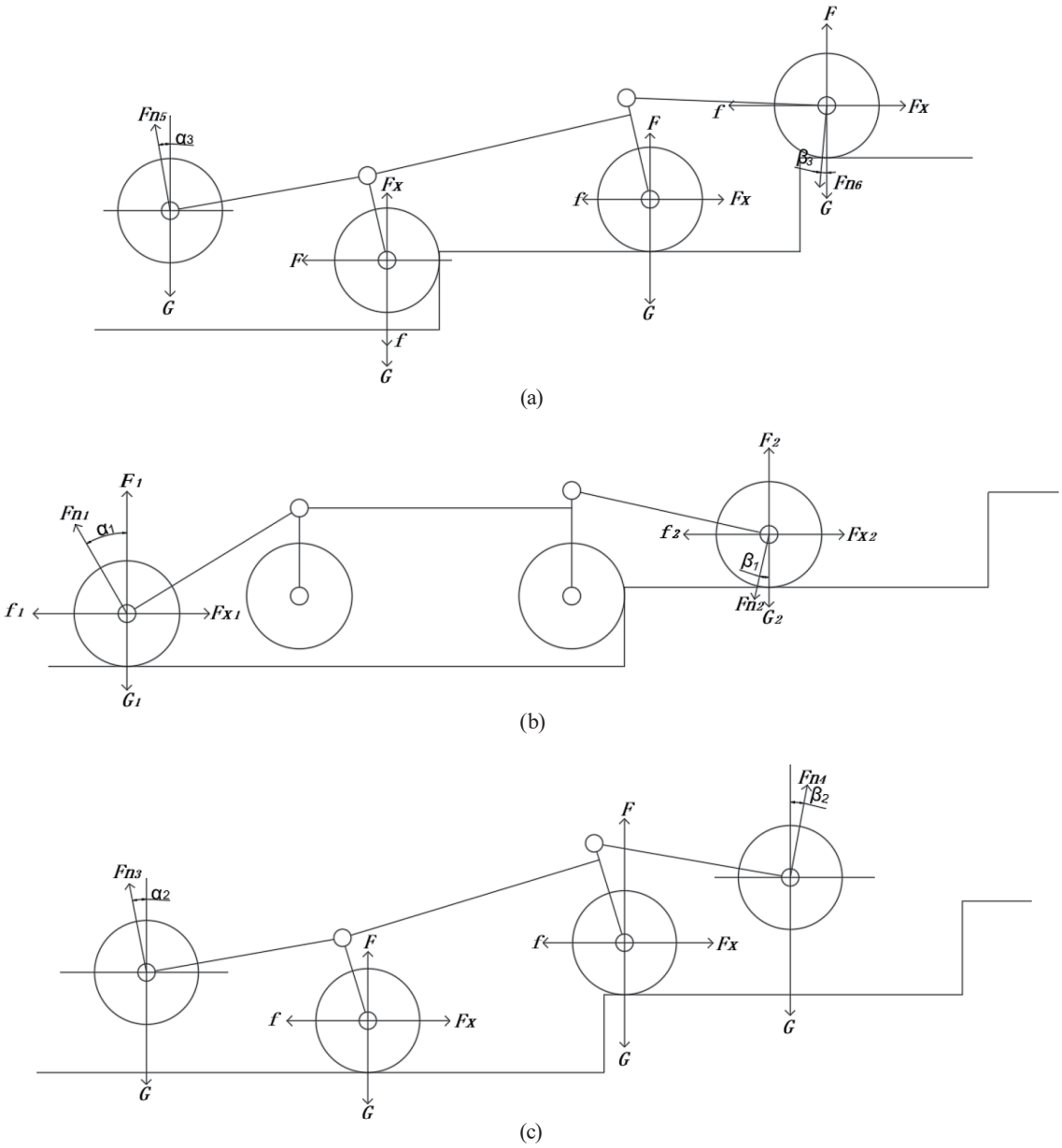

Fig. 6. Force distributions of bionic OCV during stair-climbing process. (a) State 1: the front auxiliary arm presses down and the rear auxiliary arm begins to lift. (b) State 2: the front wheel climbs the first step. (c) State 3: the rear wheel touches the first step.

$$G_1 = G_2, F_1 = F_2, \tag{15}$$

where G_2 is the gravitational force of the front wheels, F_2 is the ground-supporting force of the rear auxiliary arm, F_{x2} is the driving force of the wheels of the rear auxiliary arm, f_2 is the horizontal friction force between the front wheels and the ground during movement, and F_{n2} is the downward press force exerted by the RC motor with an angle of β_1 to the normal line through the wheel center.

State 2 [shown in Fig. 6(b)]:

The front auxiliary arm is pressed down, the rear auxiliary arm is in the state of rising, and the front wheel of the vehicle frame is driven by a deceleration motor to contact the upper surface of the first step.

(1) For the whole vehicle, the force balance equation in the X direction can be expressed as

$$F_{n3} \cdot \sin\alpha_2 + 2f - 2F_x - F_{n4} \cdot \sin\beta_2 = 0. \tag{16}$$

(2) For the whole vehicle, the force balance equation in the Y direction can be expressed as

$$F_{n3} \cdot \cos\alpha_2 + 2F + F_{n4} \cdot \cos\beta_2 - 4G = 0, \tag{17}$$

where F is the supporting force of the ladder on the vehicle, f is the friction force between the wheel and the first-step surface or the ground, F_x is the driving force of the front or rear wheel of the vehicle frame, F_{n3} is the counteracting force applied at the rear auxiliary arm with an angle of α_2 to the normal line through the wheel center, and F_{n4} is the counteracting force applied at the front auxiliary arm with an angle of β_2 to the normal line through the wheel center.

State 3 [shown in Fig. 6(c)]:

The front auxiliary arm of the vehicle is in the state of pressing so that the wheel of the front auxiliary arm comes into contact with the upper surface of the second step.

(1) For the whole vehicle, the force balance equation in the X direction can be expressed as

$$2F_x - F_{n5} \cdot \sin\alpha_3 - F - 2f - F_{n6} \cdot \sin\beta_3 = 0. \tag{18}$$

(2) For the whole vehicle, the force balance equation in the Y direction can be expressed as

$$2F + F_x + F_{n5} \cdot \cos\alpha_3 - F_{n6} \cdot \cos\beta_3 - 4G - f = 0, \tag{19}$$

where F_{n6} is the press force on the front auxiliary arm exerted by the RC motor with an angle of β_3 to the normal line through the wheel center, F_{n5} is the counteracting supporting force of F_{n6} applied at the rear auxiliary arm with an angle of α_3 to the normal line through the wheel center, f is the friction force between the wheel and the first-step surface or the second-step surface, F_x is the driving force of the front or rear wheel of the vehicle frame, F is the supporting force applied at the wheels, and G is the gravitational force applied on the whole vehicle.

As a brief summary, through the force analysis of three different postures of the bionic OCV in the process of climbing a ladder, we can understand how the vehicle's front and rear auxiliary arms affect the vehicle motion as well as the vehicle's force balance conditions during motion.

3. Kinematic Model and Simulation Analysis of Bionic OCV

3.1 Kinematic model

The material of our designed bionic OCV is selected as iron metal, and the friction coefficients of the vehicle are set to 0.25 and 0.3 in motion and under static conditions, respectively. We used two servomotors: a constant-speed motor (set as 100 rpm) to drive the front and rear wheels, and a swinging motor (set as 45° within 2 s) to control the up and down motions of the front and rear auxiliary arms. The swinging motion of auxiliary arms can be described using a trigonometric function of cos *x* as

$$\cos\left(\left(t-0.5\right)\cdot\pi+1\right)\cdot 45. \tag{20}$$

We used a well-known D-H coordinate method[22] to derive the motion equation of the proposed bionic OCV in the ladder-climbing process. This method is based on the concept that the motion of an OCV can be expressed by the pose determined from the end-point coordinates of the vehicle shape. The kinematic equation of an OCV is expressed as

$${}^{0}T_{2} = {}^{0}T_{1}\left(\theta_1\right)\cdot {}^{1}T_{2}\left(\theta_2\right), \tag{21}$$

where ${}^{0}T_1(\theta_1)$ and ${}^{1}T_2(\theta_2)$ mean the homogeneous transformation matrices of the front and rear auxiliary arms, respectively. Moreover,

$${}^{0}T_{1}\left(\theta_1\right)=\begin{bmatrix}\cos\theta_1 & -\sin\theta_1 & 0 & a_1\\ \sin\theta_1 & \cos\theta_1 & 0 & 0\\ 0 & 0 & 1 & 0\\ 0 & 0 & 0 & 1\end{bmatrix} \tag{22}$$

and

$${}^{1}T_{2}\left(\theta_2\right)=\begin{bmatrix}\cos\theta_2 & -\sin\theta_2 & 0 & a_2\\ \sin\theta_2 & \cos\theta_2 & 0 & 0\\ 0 & 0 & 1 & 0\\ 0 & 0 & 0 & 1\end{bmatrix}, \tag{23}$$

where θ_1 and θ_2 represent the rotational angles of the front and rear auxiliary arms, respectively. Substituting Eqs. (22) and (23) into Eq. (21), we have

$$ {}^{0}T_{2} = \begin{bmatrix} \cos\theta_1\cos\theta_2 & -\cos\theta_1\sin\theta_2 & -\sin\theta_1 & a_1\cos\theta_1 \\ \sin\theta_1\cos\theta_2 & -\sin\theta_1\sin\theta_2 & \cos\theta_1 & a_2\sin\theta_1 \\ -\sin\theta_2 & -c\cos\theta_2 & 1 & 0 \\ 0 & 0 & 0 & 1 \end{bmatrix}. \quad (24) $$

The shape of the OCV in motion can be completely determined using Eq. (24).

3.2 Simulation results and analysis of motion trajectory

Through simulations using ADAMS software,[9] we obtained the motion trajectory of a point on the wheel of the front auxiliary arm, and the results are shown in Fig. 7. It is seen that, in total, the vehicle moves backward twice during the climbing process because of jamming. The reason is that when the OCV moves to the position where its front auxiliary arm is located on the same horizontal staircase as the front wheel, the front auxiliary arm is too long and will push the body backward when it swings upward, causing the truck phenomenon.

Through simulations via the Matlab software, the contact forces between the front auxiliary arm wheel and the ladder and the rear auxiliary arm wheel and the ladder along the moving direction are obtained, as shown in Figs. 8(a) and 8(b). We find that the maximum contact force between the front auxiliary arm wheel and the ladder is N_1 = 48 N, whereas the maximum contact force between the rear auxiliary arm wheel and the ladder is N_2 = 0.4 N, which indicates that the obstacle crossing process of the designed bionic OCV is mainly accomplished by the front auxiliary arm, and the rear auxiliary arm mainly acts as a vehicle-body stabilizing component.

4. FEA of Easily Worn Parts

During the obstacle-climbing motion of the proposed OCV, its front and rear auxiliary arms are constantly swinging up and down, causing rapid changes in the force on the RC motor. This can easily lead to significant wear on the motor's rudder. To optimally design a high-rigidity rudder with less material, we now calculate the stress as well as the deformation distribution of the motor rudder via FEA.[20]

In the calculations, we selected 2024-T4 aluminum alloy as the rudder material and set the applied torque as 4.4 Nm, transmitted from the wheel shaft. Eventually, we obtained

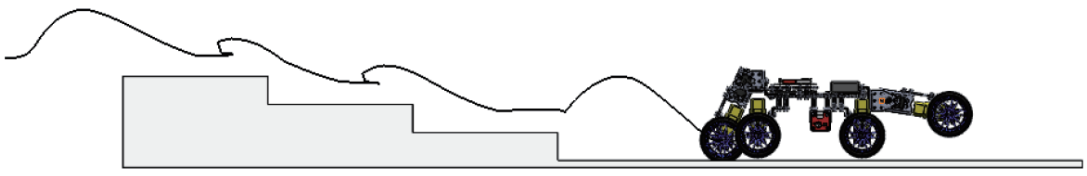

Fig. 7. (Color online) Motion trajectory of a point on the wheel of the front auxiliary arm.

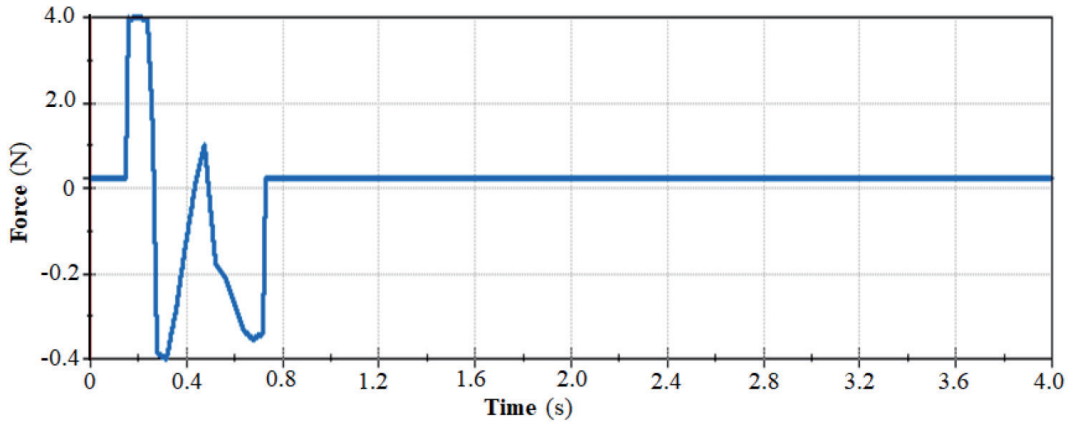

(a)

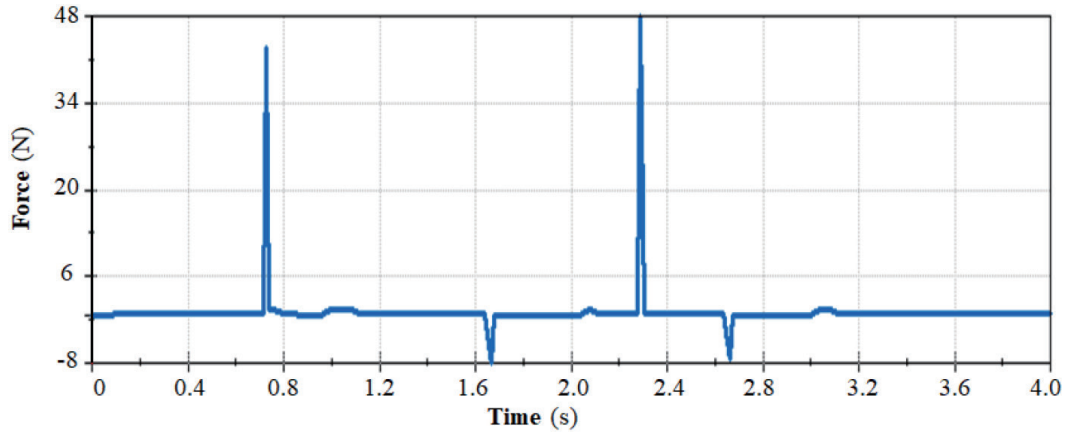

(b)

Fig. 8. (Color online) Contact forces (a) between the front auxiliary arm wheel and the ladder and (b) between the rear auxiliary arm wheel and the ladder.

the stress distribution of the rudder, as shown in Fig. 9. The maximum stress of 191.6 MPa occurs at the center hole of the rudder, which is far below the yielding stress of the adopted 2024-T4 aluminum alloy (325 MPa). Therefore, the proposed OCV can be safely run under various stair-climbing conditions.

Meanwhile, the static displacement distribution of the rudder is also obtained via FEA, as shown in Fig. 10. It is seen that the maximum displacement is 5.96 μm, appearing at the center hole of the rudder, and too small to be neglected.

5. Control Method

Essentially, the OCV is a complex, multijointed mobile robot. Because of the overlapping movement spaces of its movable parts, its overall motion exhibits a dynamic coupling relationship, making its control relatively complex and challenging. To effectively perform the motion control of our designed OCV, we adopted a novel compound control method that

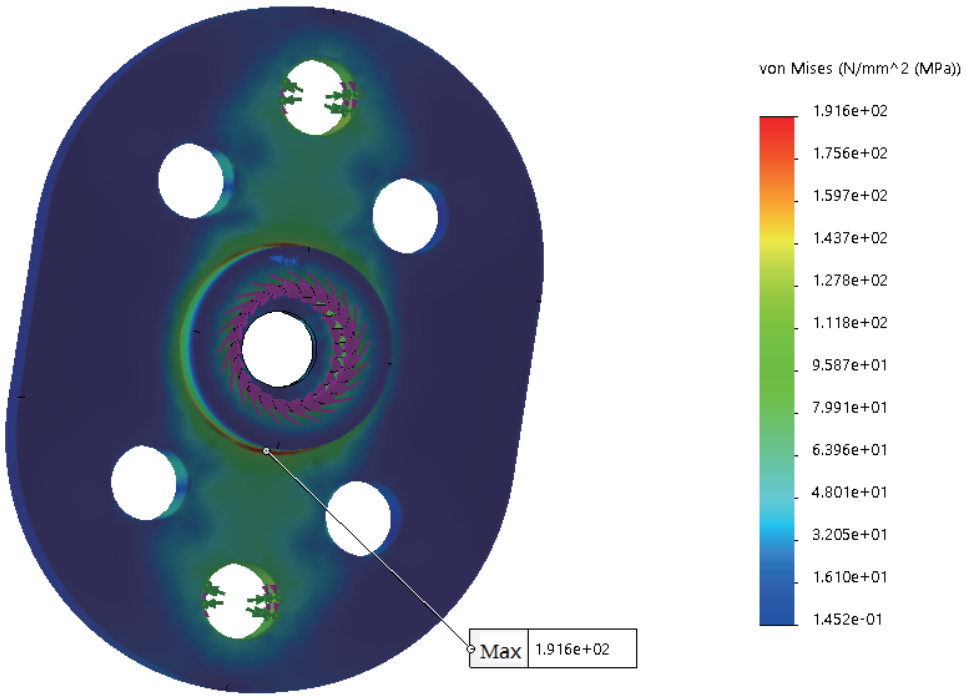

Fig. 9. (Color online) Stress distribution of rudder.

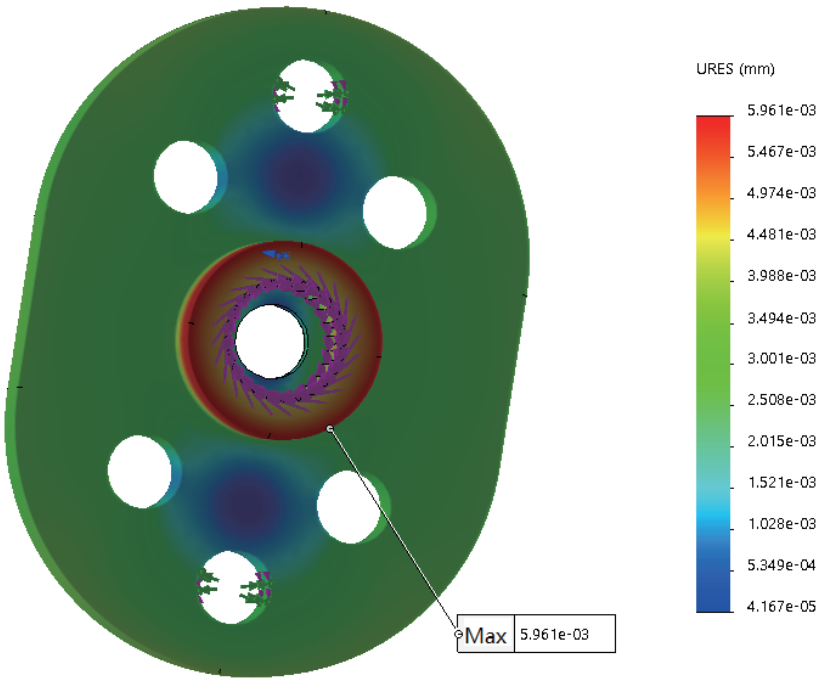

Fig. 10. (Color online) Static displacement distribution of rudder.

combines the centralized control scheme using the development control board and the hierarchical control scheme using the extension control board, as shown in Fig. 4 and mentioned earlier.

The development process of the novel composite control method proposed in this paper mainly includes secondary code development, itemized test planning, control hardware design, program burn-in, and control system optimization, as shown in Fig. 11.

In our designed bionic OCV, the front and rear auxiliary arms are the major tools to accomplish the bionic obstacle-crossing motion. The auxiliary arms swing up and down through the torque provided by the RC motor to complete the climbing action. The RC motor is composed of position sensors, gear, coreless motor, circuit board, and housing. In the control process, the output signal is sent back to the input signal for comparison to form a closed-loop feedback system. The RC motor receives the feedback signal, determines the rotation direction through the integrated circuit chip, drives the coreless motor to start rotating, transmits the power to the auxiliary arm through the reduction gear, and then sends a signal back through the position sensor to determine whether the auxiliary arm has reached the required position.

6. Prototype Testing

To test and verify the functions of our proposed small bionic OCV, we conducted experiments on seven different types of terrain: hill climbing, grass traversing, nonslip strip running, grid traversing, tunnel traversing, trench traversing, and ladder climbing.

The first experiment is a test of hill climbing. The experimental result is shown in Fig. 12(a). Our designed bionic OCV can quickly climb up and smoothly go down the hill. We find that the climbing ability can be apparently improved by properly setting the alternating swing time of the front and back auxiliary arms.

The second experiment is the test of grass traversing, which can test the driving stability of our designed bionic OCV under the influence of weeds and other foreign objects. The experimental result is shown in Fig. 12(b). We can see that the OCV does not stop or deviate from the original motion track when it crosses the grass.

The third experiment is the test of nonslip strip running, which can test the driving stability of our designed bionic OCV passing through a nonslip strip road. The nonslip strip road consists

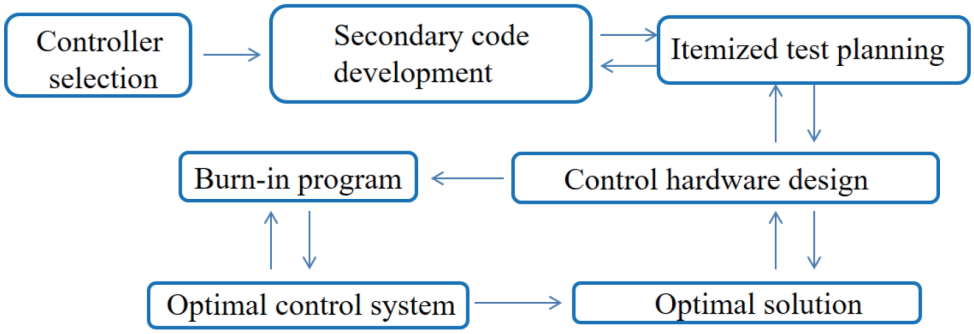

Fig. 11. (Color online) Development process of proposed composite control method.

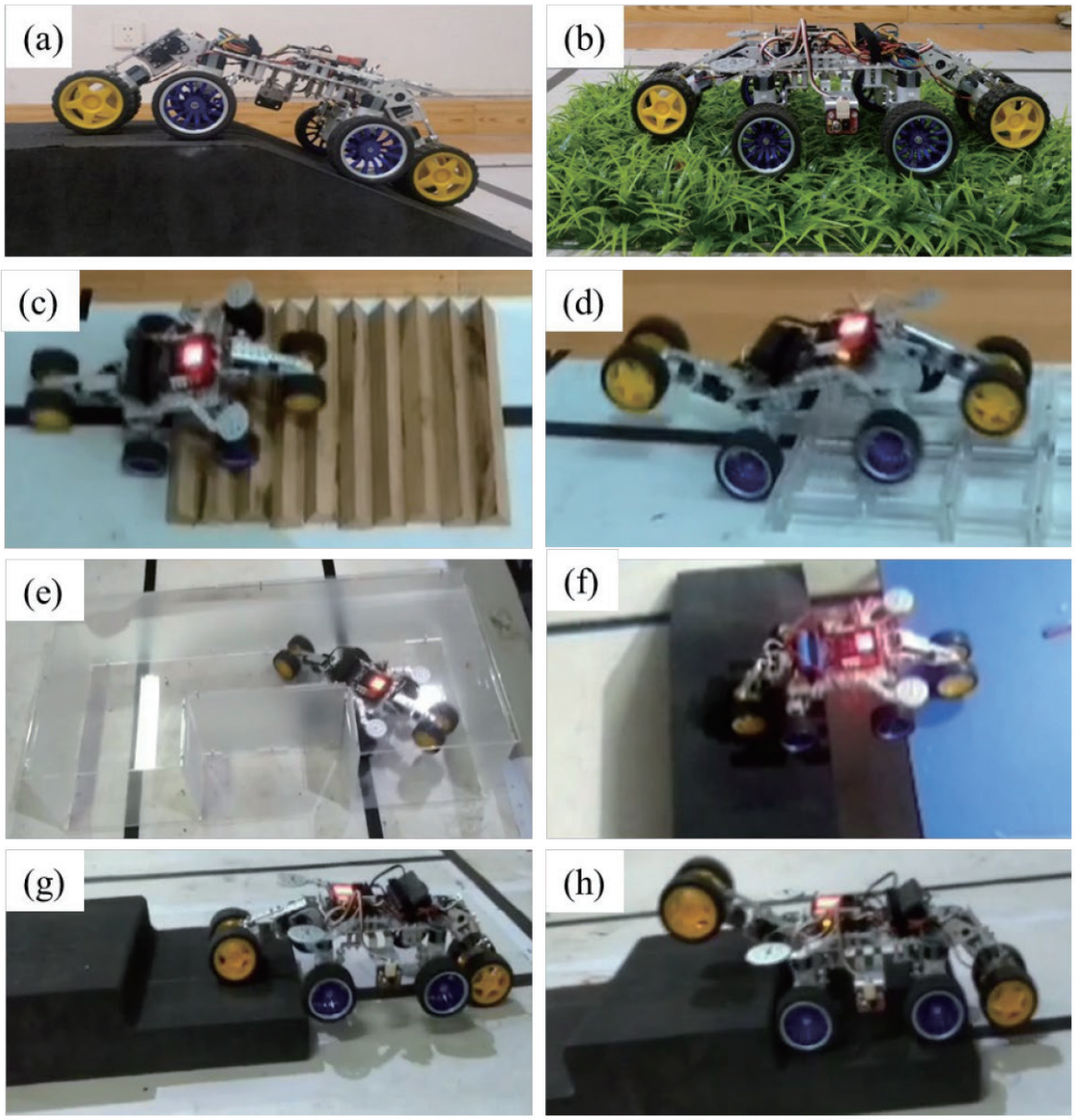

Fig. 12. (Color online) Various experimental situations of bionic OCV.

of ten triangular prisms, each 50 mm long and 30 mm high. The experimental result is shown in Fig. 12(b). We find that through the synergistic action of the front and rear auxiliary arms, the OCV can pass smoothly without pushing the nonslip strip road away from the ground.

The fourth experiment is the test of grid traversing, which can test the passage of the OCV on a very uneven road surface. The test result is shown in Fig. 12(d). The results show that when the wheel is stuck in the road grid hole, it can still pass smoothly with the help of alternating swinging of the front and rear auxiliary arms.

The fifth experiment is the test of tunnel traversing. This experiment is mainly used to verify the passage performance of the OCV in a narrow U-shaped tunnel. The U-shaped tunnel is

specially designed: the length between the inlet and the outlet is 300 mm, the height is 200 mm, the total length of the tunnel is 900 mm, and the width is 450 mm. The test result is shown in Fig. 12(e). We find that the OCV can easily enter the tunnel entrance, navigate through two U-turns without stopping, and exit the tunnel. The observation results show that the designed bionic OCV has good tunnel passing performance.

The sixth experiment is the test of trench traversing. The trench is specifically designed with a width of 150 mm and a depth of 200 mm. The test result is shown in Fig. 12(f). The bionic OCV can easily and smoothly pass through the trench without any wheel slip or jamming.

The seventh experiment is the test of ladder climbing, which mainly tests the ladder climbing ability of the OCV without wheel jamming in motion. There are two types of stairs used in this test: the first type is 25 cm long, 20 cm wide, and 54 cm high, and the second type is 30 cm long, 15 cm wide, and 50 cm high. The test result of OCV crossing the first type of ladder is shown in Fig. 12(g), and that crossing the second type of ladder is shown in Fig. 12(h). The above observation results show that the designed bionic OCV can easily and quickly complete the climbing work of various ladder heights and has good performance.

7. Conclusions

First, on the basis of the principle of bionics, we innovatively designed an OCV. The work that we performed consists of the structural design, key component selection, obstacle-crossing action planning, stress and deformation analyses via FEA, and OCV prototype development. The novelty of our designed OCV is that it has a multistage body structure with auxiliary arms, exhibiting high ladder-climbing and barrier-crossing abilities. Second, we proposed a compound obstacle-crossing control method that is highly adaptive to different environments with various obstacles and has high performance in obstacle-crossing motion control. Third, we carried out experimental tests for seven types of road condition with different obstacles. The test results showed that our designed bionic OCV with the compound control method exhibits good maneuverability and obstacle-crossing ability for different terrains of roads. Moreover, we found that the alternating swinging frequency or time of the front and rear auxiliary arms has a significant effect on the vehicle's obstacle-crossing performance. In the future, we intend to develop more bionic-based OCVs and their suitable control methods that allow them to adapt to different rescue missions with roads of different types of terrain.

Acknowledgments

This work was supported by the Special Project of the Central Government to Guide Local Scientific and Technological Development under Grant no. 2021L3046, the Project of the Department of Science and Technology of Fujian Province, China (Grant nos. 2021G02013, 2020H0049, and 2021H0060), and in part by Sanming University of Fujian Province, China (Grant nos. 19YG05 and 19YG04).

References

1 M. Tanaka, M. Nakajima, Y. Suzuki, and K. Tanaka: IEEE/ASME Trans. Mechatron. **23** (2018) 531. https://doi.org/10.1109/TMECH.2018.2792013
2 Y. Chen, D. Wang, H. Zhong, Y. Zhu, J. Yang, and C. Wang: J. Adv. Comput. Intell. Intell. Inf. **26** (2022) 355. http://doi.org/10.20965/jaciii.2022.p0355
3 J. Guo, H. Gao, L. Ding, T. Guo, and Z. Deng: J. Terramech. **70** (2017) 49. https://doi.org/10.1016/j.jterra.2017.01.004
4 T. Omura and G. Ishigami: J. Rob. Mechatron. **29** (2017) 902. https://doi.org/10.20965/jrm.2017.p0902
5 D. Chugo, K. Kawabata, H. Kaetsu, H. Asama, T. Mishima, and K. Takase: 2008 SICE Annual Conf. (2008) 695. http://doi.org/10.1109/SICE.2008.4654745
6 Z. Luo, J. Shang, and Z. Zhang: J. Cent. South Univ. **20** (2013) 62. https://doi.org/10.1007/s11771-013-1460-8
7 M. Bjelonic, P. K. Sankar, C. D. Bellicoso, H. Vallery, and M. Hutter: IEEE Rob. Autom. Lett. **5** (2020) 3626. https://doi.org/10.1109/LRA.2020.2979661
8 J. Kim, J. Kim, and D. Lee: J. Mech. Sci. Technol. **32** (2018) 5389. https://doi.org/10.1007/s12206-018-1037-4
9 K. Xu, Y. Lu, L. Shi, J. Li, S. Wang, and T. Lei: Mech. Mach. Theory **181** (2023) 105199. https://doi.org/10.1016/j.mechmachtheory.2022.105199
10 M. He, X. Yue, Y. Zheng, J. Chen, S. Wu, Z. Heng, X. Zhou, and Y. Cai: Robotica **41** (2023) 2625. https://doi.org/10.1017/S0263574723000577
11 S. Zhang, J. Yao, and L. Fu: 2021 IOP Conf. Ser.: Mater. Sci. Eng. **1043** (2021) 042032. https://doi.org/10.1088/1757-899X/1043/4/042032
12 W. Wang, X. Xu, H. Xu, and C. Sun: Proc. IMechE Part C: J. Mech. Eng. Sci. **235** (2020) 1. https://doi.org/10.1177/0954406220951600
13 C. Wang, S. Wang, H. Ma, H. Zhang, X. Xue, H. Tian, and L. Zhang: Appl. Sci. **12** (2022) 10526. https://doi.org/10.3390/app122010526
14 K. Xu, J. Li, J. Si, Y. Liu, and M. Nie: Machines **11** (2023) 1. https://doi.org/10.3390/machines11060650
15 H. Chen and Z. Yu: Acta Armamentarii **35** (2014) 1696. https://doi.org/10.3969/j.issn.1000-1093.2014.10.026
16 D. Leng, S. Shao, Y. Xie, H. Wang, and G. Liu: Ocean Eng. **228** (2021) 108565. https://doi.org/10.1016/j.oceaneng.2020.108565
17 W. Hao, X. Xu, H. Xu, and F. Zhou: 2019 IEEE/ASME Int. Conf. Advanced Intelligent Mechatronics (2019) 1329. http://doi.org/10.1109/AIM.2019.8868337
18 A. B. Essaidi, M. Haddad, and H. E. Lehtihet: Mech. Mach. Theory **169** (2022) 104605. https://doi.org/10.1016/j.mechmachtheory.2021.104605
19 L. Ni, L. Wu, and H. Zhang: Mech. Mach. Theory **175** (2022) 104966. https://doi.org/10.1016/j.mechmachtheory.2022.104966
20 K. Xu, S. Wang, B. Yue, J. Wang, H. Peng, D. Liu, Z. Chen, and M. Shi: Mechatronics **69** (2020) 102388. https://doi.org/10.1016/j.mechatronics.2020.102388
21 P. K. Behera and A. Gupta: J. Mech. Sci. Technol. **32** (2018) 4903. https://doi.org/10.1007/s12206-018-0938-6
22 D. K. Hong, W. Hwang, J. Y. Lee, and B. C. Woo: IEEE Trans. Magn. **54** (2018) 1. http://doi.org/10.1109/TMAG.2017.2752080